UNIVERSIDADE DE SÃO PAULO
ESCOLA DE ENGENHARIA DE SÃO CARLOS

Marcos Vítor de Rosa Jacinto da Silva

Aerodynamic Effect of a Wingtip-Mounted Propeller

São Carlos

2021

Marcos Vítor de Rosa Jacinto da Silva

Aerodynamic Effect of a Wingtip-Mounted Propeller

Monograph presented to the Aeronautical Engineering department of the São Carlos School of Engineering at the University of São Paulo as requirement for the obtainment of the title of Aeronautical Engineer.

Advisor: Prof. Dr. Fernando Martini Catalano

FINAL VERSION

São Carlos

2021

Index card prepared by User Service at “Prof. Dr. Sergio Rodrigues Fontes Library” at EESC/USP

S586a

Silva, Marcos Vítor de Rosa Jacinto da
Aerodynamic effect of a wingtip mounted propeller / Marcos Vítor de Rosa Jacinto da Silva; advisor Fernando Martini Catalano. -- São Carlos, 2021.

Monography Bachelor Final Thesis (Undergraduate in Aeronautics Engineering) -- São Carlos School of Engineering, at University of São Paulo, 2021.

1. Propellers. 2. Wingtip vortex. 3. Induced drag. 4. Distributed electric propulsion. I. Título.

Prepared by Eduardo Graziosi Silva – CRB 8/8907

FOLHA DE APROVAÇÃO

Candidato: Marcos Vítor de Rosa Jacinto da Silva
Título do TCC: Aerodynamic Effect of a Wingtip-Mounted Propeller
Data de defesa: 22/07/2021

Comissão Julgadora	**Resultado**
Professor Doutor Hernan Dario Ceron Muñoz	Aprovado
Instituição: EESC **-** SAA	
Alysson Kennerly Colaciti	Aprovado
Instituição: Embraer -	

Presidente da Banca: Professor Doutor Hernan Dario Ceron Muñoz

P/ 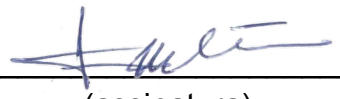

(assinatura)

ACKNOWLEDGEMENTS

First and foremost, I would like to thank my family for all the support provided to me throughout my education. I will always be grateful for having you in my life.

I thank my mentor, Fernando Martini Catalano, for orientating me in this research, Leandro Guilherme Crenite Simões, for supporting me with regards to the computational tool applied in this work, and the researchers at the Laboratório de Aerodinâmica Experimental, for the aerodynamics discussions that helped me write this report.

“The lesson I’ve learned the most often in life
is that you’re always going to know more
in the future than you know now”
Taylor Swift

ABSTRACT

Silva, Marcos Vitor de Rosa Jacinto da. **Aerodynamic effect of a wingtip-mounted propeller**. 2021. 55p. Monograph (Completion of Course Work) - São Carlos School of Engineering, University of São Paulo, São Carlos, 2021.

This work aims to investigate the aerodynamic effects of wingtip-mounted propellers on a low aspect ratio wing in cruise for a distributed electric propulsion aircraft concept. This study was carried out using Computational Fluid Dynamics (CFD) simulations with the Lattice-Boltzmann Method (LBM) and the application of collision models to predict the flow's behavior. Initially, the performance of a conventional wing is compared with a wing with a tip-mounted commercial propeller installed. The wingtip propeller can weaken the intensity of the wingtip vortex, thus leading to a more efficient wing as less induced drag is generated. The flow field around the tip is analyzed to understand the mechanisms behind the improvement. It is shown that the propeller failed to induce axial and tangential velocities at low radius, meaning further aerodynamic gains could be obtained. A customized propeller with higher loading near its hub is proposed and simulated. The new design proved to be more efficient, as it was able to generate higher lift coefficient and lower drag coefficient for fixed angles of attack. The flow structures between the configurations are compared and topics for future works on the effects of wingtip-mounted propellers of distributed electric propulsion concepts are suggested.

Keywords: Propellers. Wingtip vortex. Induced drag. Distributed electric propulsion.

RESUMO

Silva, Marcos Vitor de Rosa Jacinto da. **Aerodynamic effect of a wingtip-mounted propeller**. 2021. 55p. Monograph (Completion of Course Work) - São Carlos School of Engineering, University of São Paulo, São Carlos, 2021.

Este trabalho investiga os efeitos aerodinâmicos na instalação de hélices de ponta de asa em uma asa de baixo alongamento voltada para uma aeronave com distribuição elétrica distribuída em operação de cruzeiro. O estudo foi realizado usando *Computational Fluid Dynamics* (CFD) com o método Lattice-Boltzmann e modelos de colisão para prever o comportamento do escoamento. Inicialmente, o desempenho de uma asa convencional é comparado com o de uma asa com um modelo comercial de hélice instalado em sua ponta. A hélice reduz a intensidade do vórtice de ponta de asa, levando a uma asa mais eficiente, uma vez que menos arrasto induzido é gerado. O campo de escoamento ao redor da asa é analisado para o entendimento dos mecanismos por trás deste efeito. É mostrado que a hélice não induz velocidades axial e tangencial em baixos raios, logo, é possível obter ganhos aerodinâmicos ainda maiores. Uma hélice personalizada com mais carregamento próximo ao seu centro é proposta e simulada. A nova hélice mostrou ser mais eficiente e gerou valores maiores de sustentação e valores menores de arrasto para os ângulos de ataque analisados. As estruturas do escoamento são comparadas entre as três configurações e tópicos para trabalhos futuros sobre o efeito de hélices de ponta de asa em propulsão elétrica distribuída são sugeridos.

Palavras-chave: Propellers. Wingtip vortex. Induced drag. Distributed electric propulsion.

LIST OF FIGURES

LIST OF TABLES

LIST OF ABBREVIATIONS AND ACRONYMS

APC	Advanced Precision Composite propellers
CAD	Computer Aided Design
CFD	Computational Fluid Dynamics
LAE	Laboratório de Aerodinâmica Experimental (Experimental Aerodynamics Laboratory)
LBM	Lattice-Boltzmann Method
NASA	National Aeronautics and Space Administration
RNG	Re-normalization group
UAV	Unmanned Air Vehicle
VTOL	Vertical Take-Off and Landing
WF	Wing + Tip Fairing configuration
WFP_C	Wing + Tip Fairing + Commercial Propeller configuration
WFP_O	Wing + Tip Fairing + Optimized Propeller configuration

LIST OF SYMBOLS

α	Geometric angle of attack [deg]
α_{eff}	Effective angle of attack [deg]
α_i	Induced angle of attack [deg]
α_L	Local angle of attack [deg]
AR	Aspect Ratio [-]
β	Geometric angle at a blade section [deg]
b	Wing semi-span [m]
C_D	Drag Coefficient [-]
C_{D_0}	Parasite Drag Coefficient [-]
C_{D_i}	Induced Drag Coefficient [-]
C_l	2D Lift Coefficient [-]
C_L	Lift Coefficient [-]
C_p	Pressure Coefficient [-]
C_T	Thrust Coefficient [-]
e_0	Owswald efficiency number [-]
$e_0 AR$	Effective Aspect Ratio [-]
$k-\epsilon$	k-epsilon turbulence model
L/D	Aerodynamic Efficiency [-]
R	Propeller Radius [m]
Re	Reynolds Number [-]
T	Thrust
v_a	Axial velocity induced by a propeller [m/s]
v_t	Tangential velocity induced by a propeller [m/s]
V_∞	Free-Stream Velocity
w	Downwash [m/s]

CONTENTS

1 INTRODUCTION

Propellers are used for generating thrust since the beginning of aviation and, with the technological development of electrical engines, the integration of propellers in non-conventional configurations to achieve new applications became possible (MOORE; FREDERICKS, 2014). An example of this is the distributed electrical propulsion concept, in which several propellers are distributed upstream of the wing to locally accelerate the flow and increase the generation of lift. These concepts often employ wingtip mounted propellers, responsible for cruise propulsion and decreasing induced drag. Those technologies are specially attractive for Unmanned Air Vehicles (UAVs), Vertical Take-Off and Landing aircraft (VTOL) and urban air mobility projects. The X-57 Maxwell, shown on figure 1, is a project under development at NASA to prove that electric powered aircraft can be more efficient, quieter and more environmentally friendly than traditional gas powered aircraft (BORER *et al.*, 2016).

Figure 1 – X-57 Maxwell

Source: (NATIONAL AERONAUTICS AND SPACE ADMINISTRATION - NASA, 2021)

Induced drag is a consequence of the generation of wingtip vortex due to the pressure difference between the lower and upper surfaces of a wing. Conventional methods to decrease this effect consist on reducing the pressure difference near the tip by increasing the wing's Aspect Ratio or through aerodynamic torsion. The former method decreases the area of the wing on the sections close to its tip, thus reducing the lift generated at the tip. The latter uses an airfoil at the tip that generates less C_l to create the same effect. Another common solution is to use winglets. These structures are designed to generate a forward force component inside the circulation field of the vortex, decreasing its strength. Through the installation of a wingtip propeller, it is possible to decrease even further the vortex intensity as it is capable of inducing flow rotation contrary to the wingtip vortex.

A distributed electric propulsion wing concept is being investigated at the *Laboratório de*

Aerodinâmica Experimental (LAE) of the Aeronautical Engineering Department at São Carlos School of Engineering - University of São Paulo, with sponsorship from Embraer. The wing is rectangular and has 1.4 meters of span by 0.4 m of chord, resulting in an aspect ratio of 3.5. In this phase of the study, the aerodynamic effects of mounting a propeller at the wingtips is of interest. Initially, a wing with a commercial propeller is analyzed, and based on its results, a custom propeller is proposed and simulated. The analyses are carried out using SIMULIA's PowerFLOW, a CFD solver based on the Lattice-Boltzmann Method.

2 BIBLIOGRAPHIC RESEARCH

2.1 Induced drag

The induced drag is a direct consequence of the generation of lift on a wing. On its upper surface there is a low pressure region, opposed to a high pressure region on its lower surface. At the wing tips, those two regions interact as the air from the lower surface move in direction to the low pressure region, thus generating wing tip vortices as seen in figure 2. The vortex intensity is stronger near the tip and weaken towards the root. Downstream of the wing, it creates an downward velocity component: downwash (w).

Figure 2 – Wingtip vortices

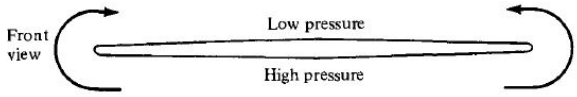

Source: (ANDERSON, 2001)

The downwash generated by the vortices induce an angle between the wing and the free stream, α_i. Therefore, the lift force generated by the wing has an induced angle with the vertical axis. The decomposition of the lift force on the horizontal direction results in the induced drag. On figure 3, a representation of the effective angle of attack on a wing is shown.

Figure 3 – Induced drag diagram

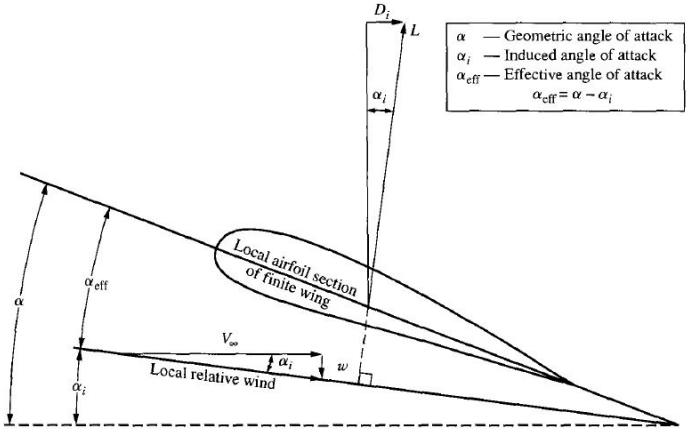

Source: (ANDERSON, 2001)

To reduce the induced drag on a wing, it is necessary to weaken the tip vortices. Installing a propeller at the wing tip, it is possible to transfer rotational energy to the flow in the opposite direction as the vortex and to generate forward thrust inside its circulation field, thus reducing the vortex intensity.

2.2 Wingtip-mounted propellers

In the 1930's, Charles Zimmerman proposed the first aircraft designs employing the usage of wingtip-mounted propellers to decrease induced drag and create uniform flow over the wing/fuselage. He developed the Vought V-173, a proof-of-concept aircraft of circular shape, with the addition of large propellers at the wingtips (figure 4). A flight test campaign proved Zimmerman's ideas were practical, as the aircraft showed good low-speed performance, however his concepts were ultimately cast aside due to the potential of high-speed performance of the turbojet engines in development at the time. (SMITHSONIAN, 2021)

Figure 4 – Vought V-173

Source: (SMITHSONIAN, 2021)

The aerodynamic effects of wingtip mounted propellers were further studied by Snyder and Zumwalt (1969) on a wing with AR = 8 and a low-pitch propeller ($\beta = 15.5°$ at $r/R = 0.6$). They proved counter-vortex turning propellers mounted at the wingtip increase lift and decrease drag. The lift benefit is a consequence mainly of the larger local angle of attack in the propeller slipstream, but also of the the larger velocity and dynamic pressure behind the propeller. The drag benefit is credited to the decrease in downwash induced by the propeller's attenuation of the wingtip vortex. Figure 5 shows the influence of a wingtip-mounted propeller on the wing's downwash.

Miranda and Brennan (1986) carried out parametric studies on a wing of $AR = 6.0$ and identified the main parameters that affects the aerodynamic performance of wingtip-mounted

Figure 5 – Effect of a wingtip-mounted propeller on downwash for pro-vortex rotation (left) and counter-vortex rotation (right)

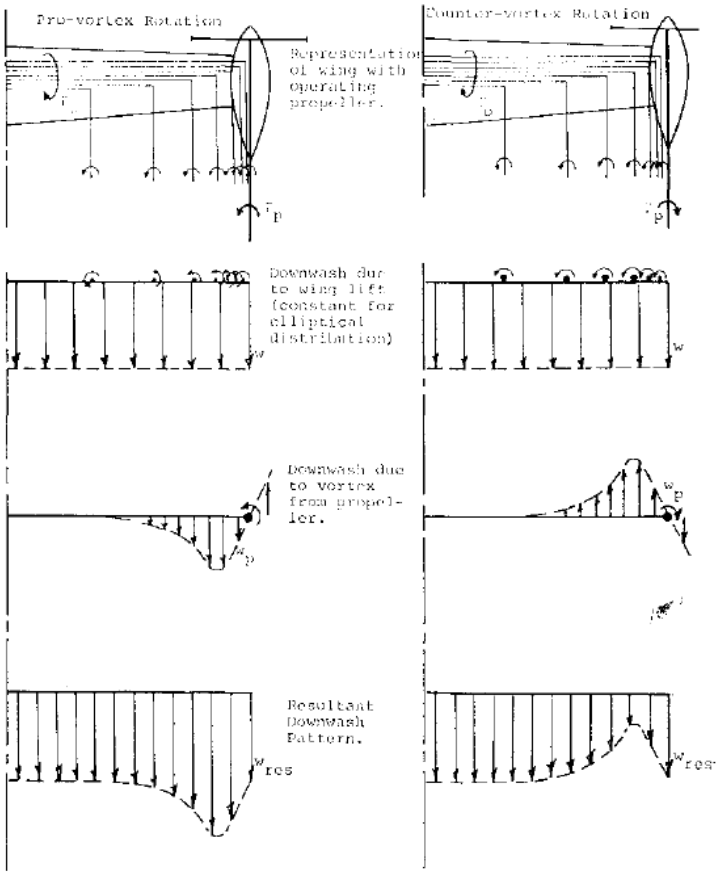

Source: (SNYDER; ZUMWALT, 1969)

propellers: tip speed to flight speed ratio and propeller diameter to wing span ratio. Higher tip speed to flight speed ratios and lower propeller diameter to wing span ratios produce larger total drag reduction, as shown on figure 6. Moreover, it was found that increasing the wing's aspect ratio, the benefit provided by wingtip-mounted propeller is decreased.

Sinnige *et al.* (2018) compared a wingtip-mounted propeller performance against a inboard mounted layout for wings with $AR \approx 6.1$. It was shown that, although presenting an increase in lift 1-4% smaller, the wingtip-mounted configuration reduces 5-15% more drag than the inboard-mounted layout for the same C_L and C_T values. The authors concluded that this drag benefit is due to the reduction of induced drag, as the wingtip-mounted propeller slipstream attenuates the wingtip vortex.

Dimchev (2012) conducted experimental simulations to determine the performance of wingtip-mounted propellers on a wing of $AR = 2.7$ at similar Re range to the one studied at LAE (Re 400.000 to 740.000). Dimchev's results show an increase in lift and a decrease in drag, however the values are not corrected for propeller thrust and the impact of the propeller on

Figure 6 – Effect of tip speed to flight ratio and propeller diameter to wing span ratio on drag reduction

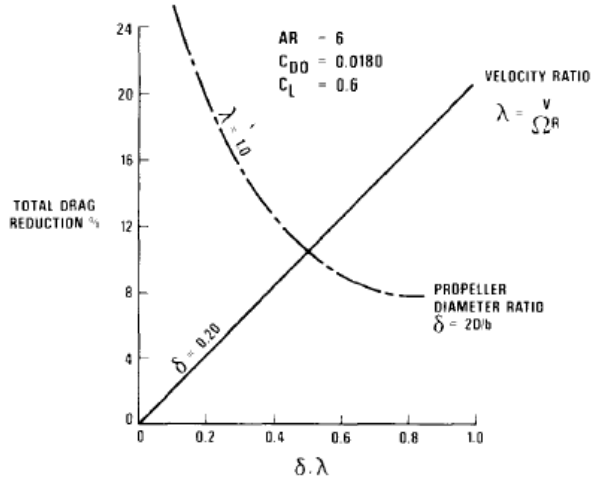

Source: (MIRANDA; BRENNAN, 1986)

induced drag or effective AR is not quantified. Moreover, through flow visualization techniques, Dimchev acquired insightful qualitative information regarding flow over the wing. In the propeller wake, separation bubbles were eliminated and the nacelle effect on the flow is minimized when the propeller is active. Dimchev also found that the distance between the leading edge and the propeller plane did not affect significantly C_L and C_D.

This research aims to analyze the impact of wingtip-mounted propellers on induced drag for a low-AR wing design and to obtain thrust corrected values of C_L and C_D. The benefit in induced drag will be compared in terms of the effective aspect ratio of the system. Furthermore, the use of a CFD tool facilitates the visualization of the flow field inside the propeller slipstream, and therefore, the qualitative assessment of such configuration.

Additionally, the mentioned studies applied "conventional" propellers in their analyses. In this work, the initial results obtained with a commercial propeller will be used to propose modifications in propeller design to further improve the benefits of wingtip-mounted propellers.

3 METHODS

To determine the aerodynamic performance and flow behavior around the wing, CFD simulations were conducted for each case. The software PowerFLOW, developed by SIMULIA, was chosen for the analyses. It is well know for simulating discrete fluid represented by particle densities in discrete space and time, this is also known as the Lattice Boltzmann Method. Traditional CFD, on the other hand, solves discrete partial differential equations, such as the Navier-Stokes equations.

3.1 Lattice-Boltzmann method

In this method, the fluid dynamics is simulated through a cubic lattice. The 3D volume elements are called Voxels, meanwhile, the surface elements that describe bodies are called Surfels. Although the voxels are required to be cubic, the surfels are calculated as the intersection of voxels with the body and therefore can represent any shape. Figure 7 shows the representation of a lattice projected onto a two-dimensional plane.

Figure 7 – Lattice example

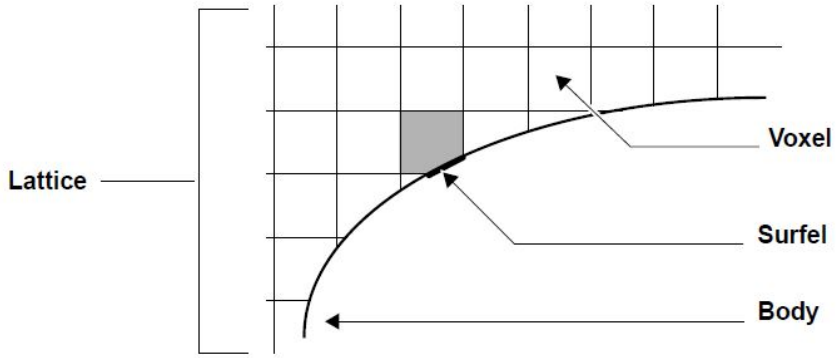

Source: (DASSAULT SYSTEMES, 2019)

Particles exist at each voxels and are allowed to move in discrete directions, at discrete velocities and discrete periods of time.

Models of microscopic processes are used to describe the interactions between particles and particles, particles and surfels, and the particles' advection.

The particle-particle interactions are calculated in two phase: At first, particles move in discrete directions from one Voxel to an adjacent one (Move Phase). Then, particles in the same voxel collide, changing velocities and directions while maintaining the total mass, momentum and energy within the voxel (Collide Phase). Such process is represented in figure 8.

Figure 8 – Particle-Particle interaction

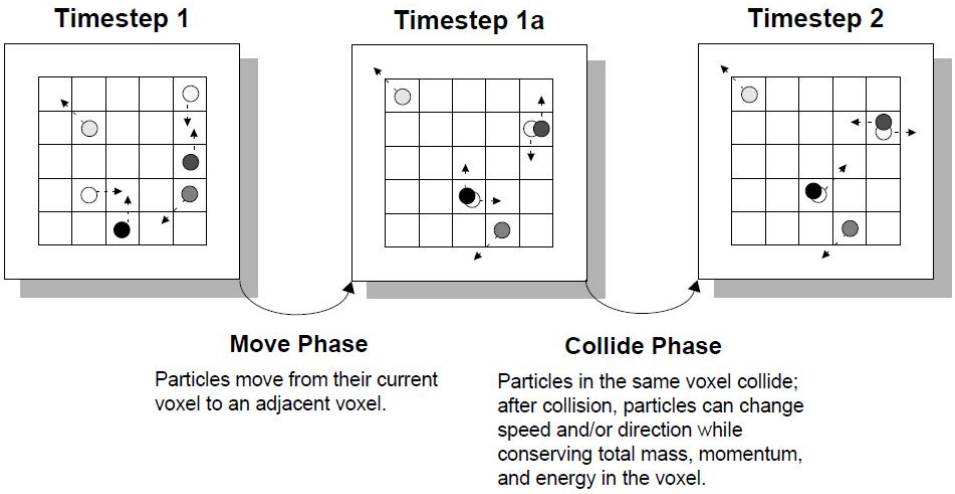

Source: (DASSAULT SYSTEMES, 2019)

In the particle-surfel interaction, the particles that would hit the surfel in a given timestep are gathered at the surfel. Then the boundary condition at given surfel is applied to the particles through a surface-collision process and the particles are released back to the fluid voxels. The surface-collision process enforce conservation mass and exchange of momentum and energy in a way that is consistent with the selected boundary condition.

For high Reynolds Number simulations (Re > 100,000), PowerFLOW employs the re-normalization group (RNG) form of the k-epsilon equations turbulence model for approximating the flow near the walls. Additionally, PowerFLOW uses the law of the wall profile coupled with the wall model pressure gradient extension to calculate skin friction.

The nature of the methods in PowerFLOW allows for faster and more computationally efficient unsteady simulations when compared to traditional CFD, based on the Navier-Stokes equations. (DASSAULT SYSTEMES, 2019).

3.2 Aerodynamics analysis

The PowerFLOW simulations will give as results the forces acting on the wing and propeller, therefore, graphs of C_L, C_D, L/D can be constructed to compare aerodynamic performance between the configurations. Furthermore, pressure coefficient plots, velocity contours, and streamlines can be elaborated to understand the flow mechanisms that are affecting performance.

It's common to relate the overall drag coefficient of a wing with its lift coefficient through

the following equation:

$$C_D = C_{D_0} + \frac{C_L^2}{\pi e_0 AR} \tag{3.1}$$

Therefore, plotting $C_D \; vs. \; C_L^2$, it's possible to determine how the propeller affects the $e_0 AR$ term in equation 3.1 analyzing the curve's derivative. This term is referred to as *effective Aspect Ratio*.

4 ANALYSIS

Firstly, the CAD geometries for simulation are prepared. The initial geometry configuration consist of a rectangular semi-wing of 0.4 x 0.7 m^2 with the LAE 2319 airfoil and a tip fairing for the installation of the propeller - WF. The WF configuration serves as the base to which the propeller effects on the aerodynamics are compared. Then, a propeller is added to the geometry, resulting in configuration WFP_C. The commercial propeller APC Sport 14x13 is selected for this configuration due to its high pitch. The WFP_C configuration is shown in figure 9. Figure 10 shows the geometry of the WF configuration. The propeller geometry is shown in figure 11.

Figure 9 – WFP_C geometry

(a) Front View

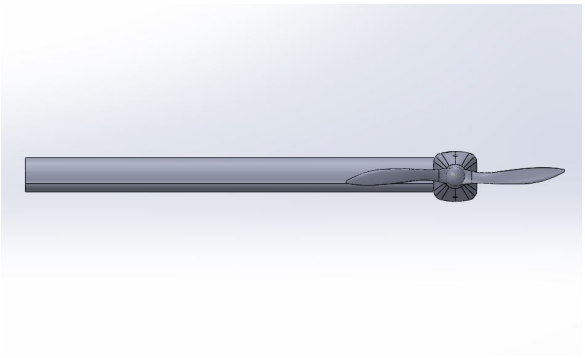

(b) Side View

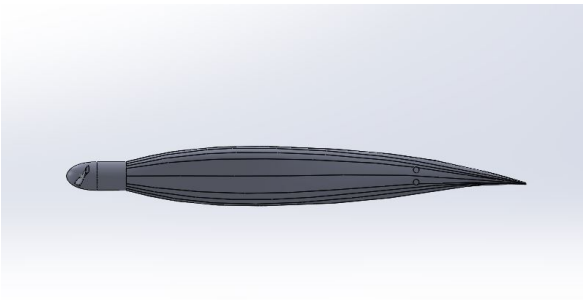

(c) Top View

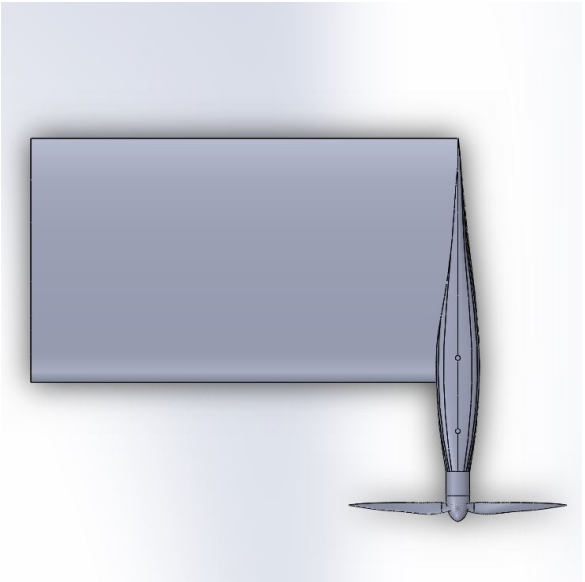

(d) Isometric View

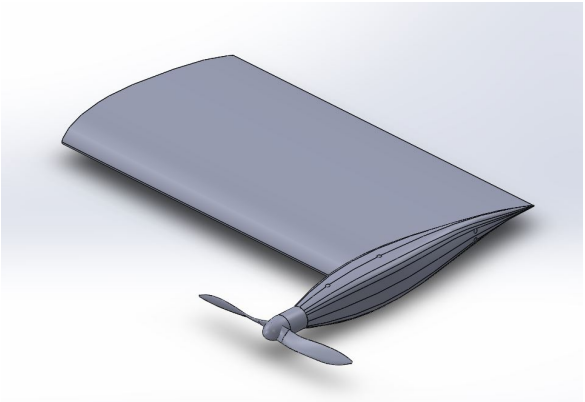

Source: Created by the author

Having set the geometries for analysis, it's important to elaborate a simulation matrix

Figure 10 – WF geometry

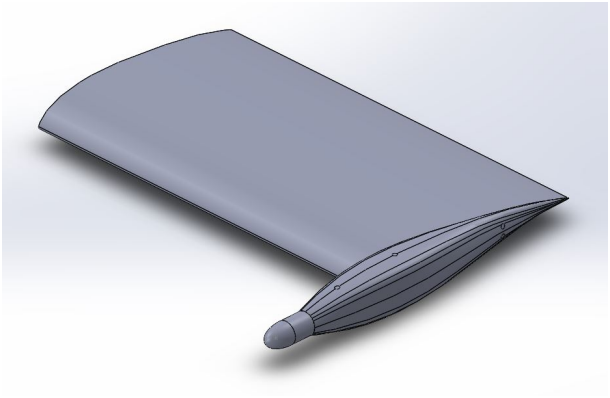

Source: Created by the author

Figure 11 – APC 14x13 geometry

(a) Front View

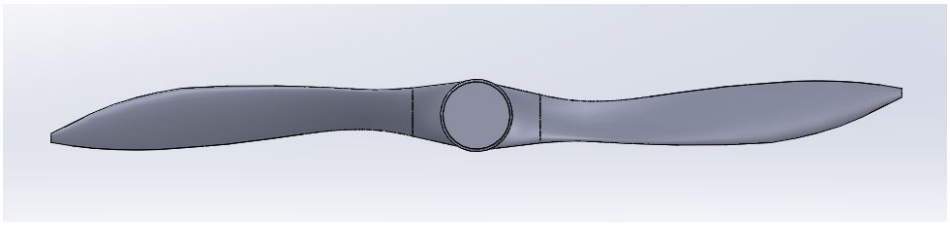

(b) Bottom View

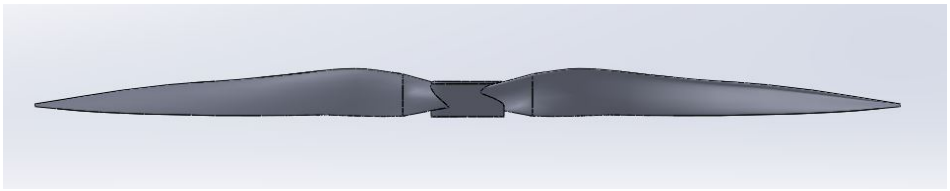

Source: Created by the author

defining the conditions to be simulated (table 1). The cruise contributes to most of an aircraft's flight duration, therefore, this is the phase of flight in which the reduction of induced drag will have the bigger impact. The cruise velocity is set to be 28 m/s. During cruise, the aircraft flies with small angle of attack, therefore simulations will be performed for α = $0°$, $5°$ and $10°$.

The propeller rotation is set so that its advance ratio is close to 1.0. For a 14 inch propeller with 2 blades and a velocity of 28 m/s, such rotational speed is 4750 rpm.

The quantitative results extracted from each simulation are force coefficients on the wing plus fairing (C_L, C_D) and the Thrust (T) generated by the propeller.

Table 1 – Simulation matrix

Sim ID	Configuration	V_∞ [m/s]	Prop. RPM [rpm]	α [deg]
01	WF	28	-	00
02	WF	28	-	05
03	WF	28	-	10
04	WFP_C	28	4750	00
05	WFP_C	28	4750	05
06	WFP_C	28	4750	10

Source – Created by the author.

4.1 Mesh independence and physics setup

Before running simulations for all conditions, it is crucial to perform a mesh independence study to ensure that the refinement applied to the mesh is not affecting the quality of the results. For this analysis, the WF configuration is chosen. The propeller rotation introduces complex phenomena to the flow, making it unpractical for a mesh independence study. Furthermore, the meshes will be tested at $\alpha = 0°$ to avoid flow separation.

A refinement pattern is fixed for this analysis, and the minimum voxel volume is reduced in multiples of 2, creating meshes with approximately the double of voxels between changes. There are 9 different refinement levels in each mesh. Sensitive regions such as the wing, the fairing and the wing wake have finer voxels than the far field. In total, 8 grids were analyzed.

It is important to mention that PowerFLOW does not generate surface meshes and it is only possible to set volumes of refinement. For this reason, it is unreasonable to fully resolve the boundary layer for high Reynolds Number cases, Re > 100,000. Thus, the solver employs turbulence modelling for both the bulk fluid and near the wall. (DASSAULT SYSTEMES, 2019)

The results from the simulations are available on table 2 and on figure 12. From Mesh ID 05 to 07, there is a difference of 0.4% for the C_L value, and of 1.0% for the C_D. However, mesh 07 has a higher computational cost and takes 189% more time to be completed. Therefore, the meshing settings of mesh 05 were selected to perform the flow simulations in this research. The selected mesh is highlighted on table 2 and figure 12. On figure 13, images of the final mesh and its refinement regions are shown.

Regarding the physics setup, PowerFLOW's employs the the renormalization group (RNG) form of the k-epsilon equation as turbulence model both in the bulk fluid and near the wall. It uses an extended wall model that dynamically incorporates pressure gradient effects. The solver assumes air is an ideal gas and that the processes are isothermal.

The flight condition set for the simulations is: air pressure of 1 atm, free stream velocity

Table 2 – Mesh independence results

Mesh ID	Voxel Length [mm]	C_L [-]	C_D[-]	No. Voxels [-]	Voxel Ratio [-]	Duration [h]
00	1.000	0.260	0.01364	1,807,886	1.00	0.55
01	0.794	0.252	0.01347	3,408,711	1.89	1.00
02	0.630	0.252	0.01460	6,505,184	3.60	1.14
03	0.500	0.246	0.01524	12,436,497	6.88	1.68
04	0.397	0.241	0.01536	24,224,845	13.40	2.84
05	**0.323**	**0.243**	**0.01516**	**43,578,089**	**24.10**	**4.54**
06	0.286	0.243	0.01525	62,188,544	34.40	6.20
07	0.250	0.244	0.01511	91,627,230	50.68	8.61

Source – Created by the author.

Figure 12 – Results of mesh independence analysis

(a) C_L and C_D (b) Simulation time

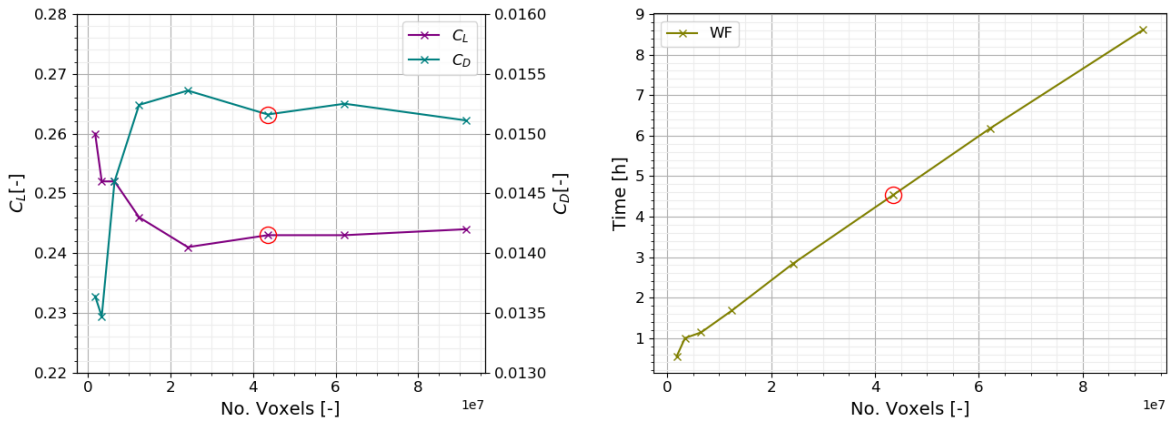

Source: Created by the author

of 28 m/s, air temperature of 300 K and air viscosity of 1.497e-05 m^2/s. This results in Mach Number equal to 0.0806 and Reynolds Number equal to 748,163. The turbulence intensity is set at 0.0021 with a turbulence length scale of 1 mm.

4.2 Performance and flow visualization

The results for the simulations conducted are shown on table 3. For better visualization of the aerodynamic properties of the two configurations, the graphs on figure 14 were elaborated.

From table 3, it is seen that the installation of the wingtip propeller increased both the lift and drag coefficients. Figures 14a and 14b complement this information, showing that, for a fixed value of C_L, lower C_D values are obtained for the WFP_C configuration. Regarding the induced drag, curve $C_D\ vs.\ C_L^2$ shows how the total drag of the aircraft relates to the lift generated. From

Figure 13 – Final mesh for simulations

(a) Mesh around wing and wake

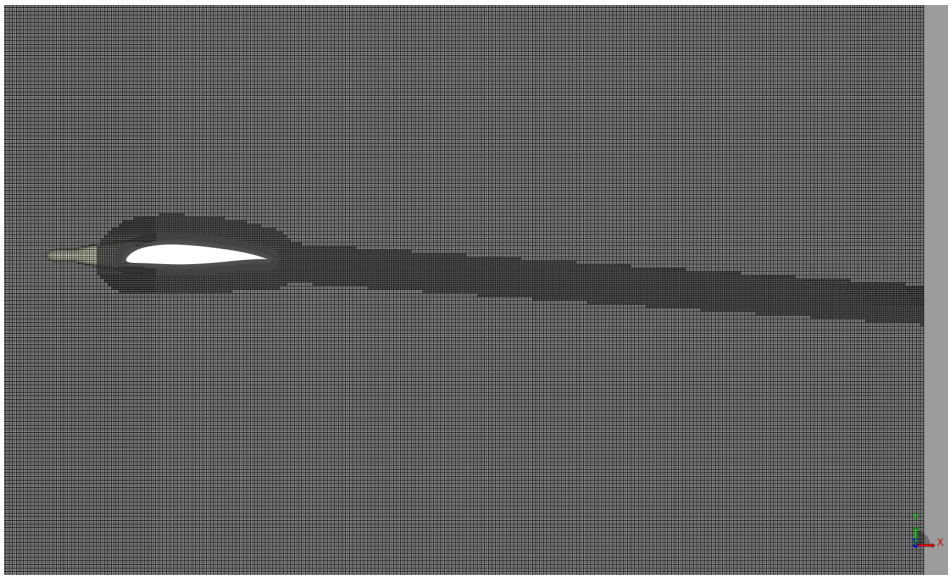

(b) Mesh at the Wingtip

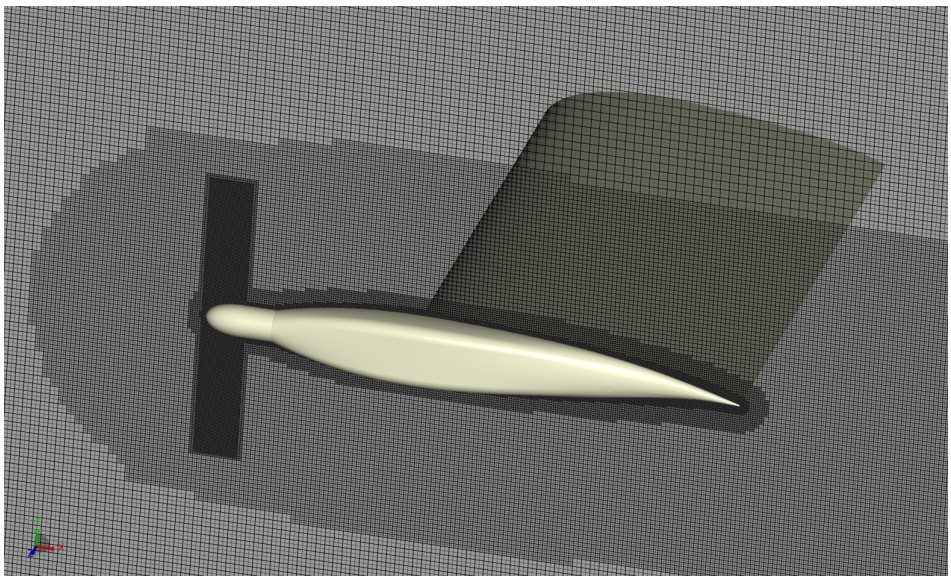

Source: Created by the author

configuration WF to WFP_C, the derivative of this curve decreased, indicating a reduction in induced drag. Figure 14d shows that the increase in lift was more significant than the increase in drag, as the lift-to-drag ratio increased for all lift coefficients obtained.

The increase in C_L occurs due to two effects: The increase in flow velocity in the propeller wake and the increase in α_L induced by the propeller slipstream. On figure 15, the lift distribution across the semi-wingspan is shown. Across the whole span, it is possible to see an increase in local lift. The offset closer to the root is generated because the wingtip vortex is weaker in the WFP_C configuration, and the lift force component has lower α_{eff}. As we move outboard, this

Table 3 – Results obtained from simulations

Sim ID	Configuration	V_∞ [m/s]	Prop. RPM [rpm]	α [deg]	C_L [-]	C_D[-]	T [N]
01	WF	28	-	00	0.24	0.0152	-
02	WF	28	-	05	0.53	0.0378	-
03	WF	28	-	10	0.80	0.0780	-
04	WFP_C	28	4750	00	0.26	0.0159	5.27
05	WFP_C	28	4750	05	0.56	0.0380	5.28
06	WFP_C	28	4750	10	0.84	0.0790	2.00

Source – Created by the author.

Figure 14 – Aerodynamic polars for WF and WFP_C

(a) C_D vs. C_L

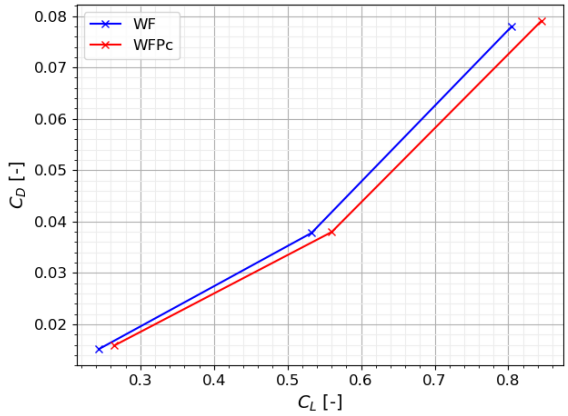

(b) C_D vs. C_L^2

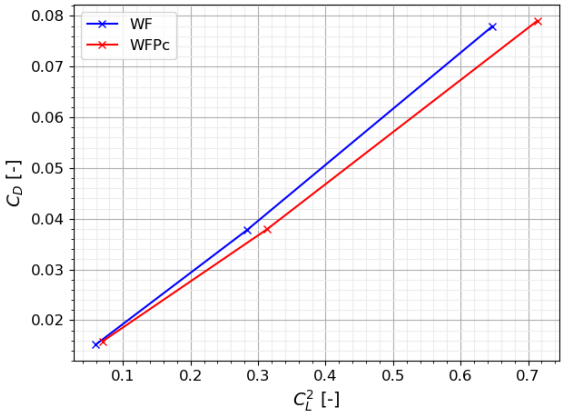

(c) C_L vs. α

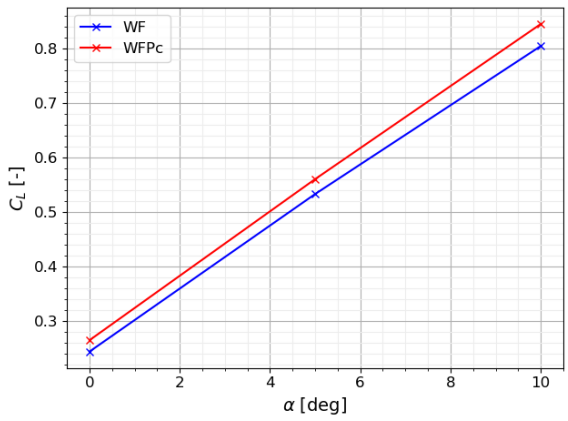

(d) L/D vs. C_L

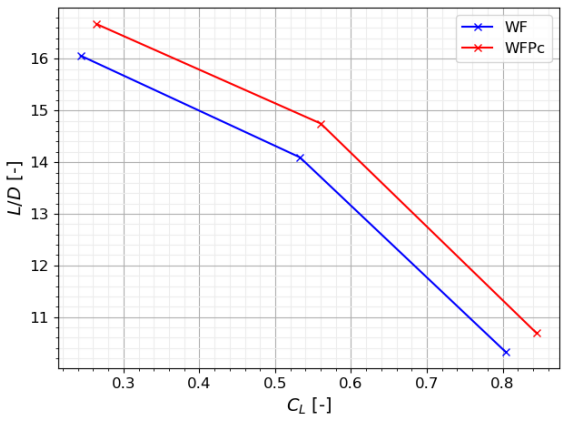

Source: Created by the author

difference increases and, directly behind the propeller wake, there is a step in lift due to the increase of the flow velocity and α_L, as seen on figure 16, which shows the local angle of attack 100 mm upstream of the leading edge for $\alpha = 0.0°$. The effect of the propeller's slipstream is

less pronounced for higher angles of attacks, because the the z-component component of the slipstream depends on $cos(\alpha)v_t - sin(\alpha)v_a$, where v_t is the tangential velocity and, v_a, the axial velocity induced by the propeller. Therefore, as α increases, the impact of the slipstream on α_L decreases. This effect can be beneficial for take-off and landing operations, as it can prevent the wing from stalling at the tip.

Figure 15 – Lift distribution for the WF and WFP_C configurations

(a) $\alpha = 0.0°$ (b) $\alpha = 5.0°$

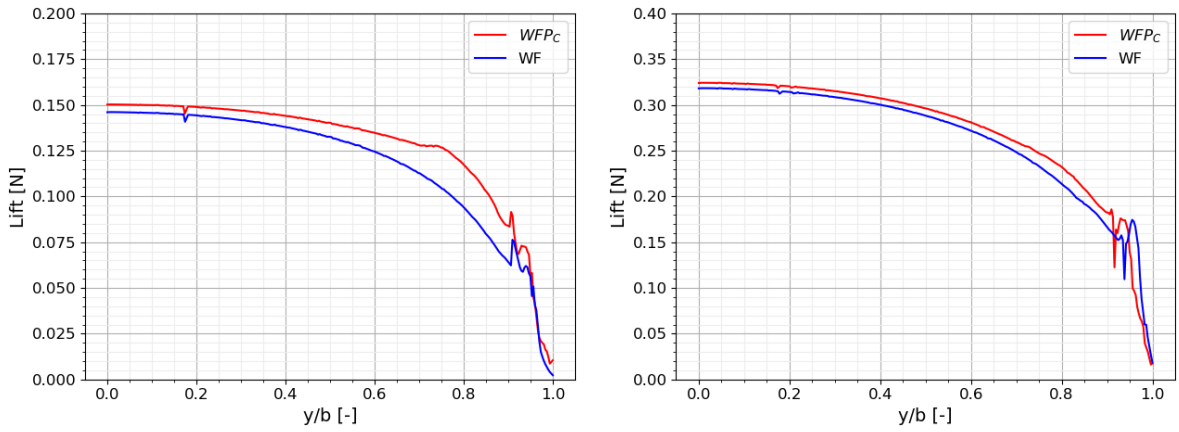

(c) $\alpha = 10.0°$

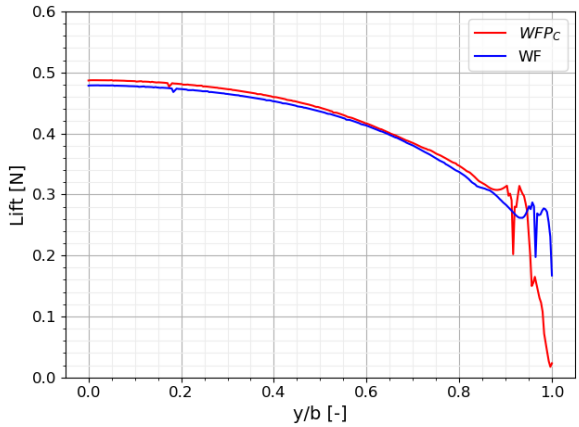

Source: Created by the author

On figure 17, the C_p is plotted across the semi-wingspan for both configurations at $\alpha = 0.0°$. Those results are in agreement with the previous discussion. Closer to the root, there are small differences for the C_p over the wing and closer to the tip, the pressure difference between the lower and upper surfaces increase.

To further understand the effect of the propeller wake, velocity contours of the flow field around the wingtip were captured for $x/c = 0.0$, $x/c = 0.5$ and $x/c = 1.0$, and $\alpha = 0.0°$ at t = 0.219932 seconds (figure 18). At $x/c = 0.0$, it is not yet possible to visualize the wingtip vortex on the WF configuration. For the WFP_C, however, it is possible to see the contra-rotating

Figure 16 – α_L 100 mm upstream of the leading edge for WF and WFP_C, $\alpha = 0.0°$

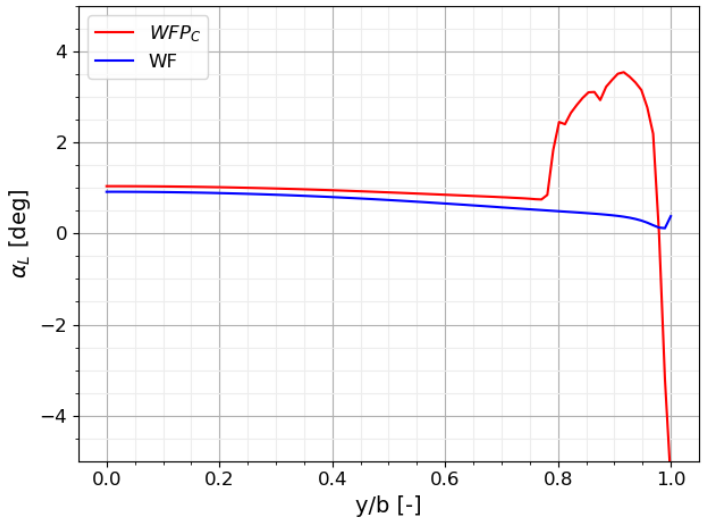

Source: Created by the author

swirl induced by the propeller in the flow field. On image 18b, vortices formed at the tips of the blade can be identified by the pressure dipoles. The flow on the propeller wake has higher velocities further away from the axis of rotation. Close to the fairing, areas of low velocities are formed, indicating losses in kinematic energy. At $x/c = 0.5$, the vortex is clearly visible on the WF configuration. As the vortex intensity is increased, on the WFP_C configuration, the vortex begins to trump the induced swirl near the fairing. For the outer regions of the wake, the propeller is still able to prevent the formation of the wingtip vortex. At $x/c = 1.0$, there is a stronger inner vortex at the wingtip of the WFP_C configuration. For the outer radius, the swirl is significantly decreased, however, in comparison with the WF configuration, still has a significant effect on weakening the wingtip vortex.

Another tool that aids in the understanding of the flow behavior are streamlines, as shown in figure 19 for $\alpha = 0.0°$. On these images, it can be seen the increased velocity in the flow and how the propeller delays the curling effect of the wingtip vortex, which also looks weaker and less structured for the WFP_C configuration.

Figure 20 shows the velocity field for its y-component at y = 0.68 m. The area in blue and red indicate the wingtip vortex. For the WF configuration, a nearly uniform vortex is formed. In contrast, for the WFP_C configuration, the vortex is weakened by the propeller and there are irregularities on the vortex stream.

Figure 17 – C_p comparison between WF and WFP_C across the wing's span for $\alpha = 0.0°$

(a) y/b = 0.0

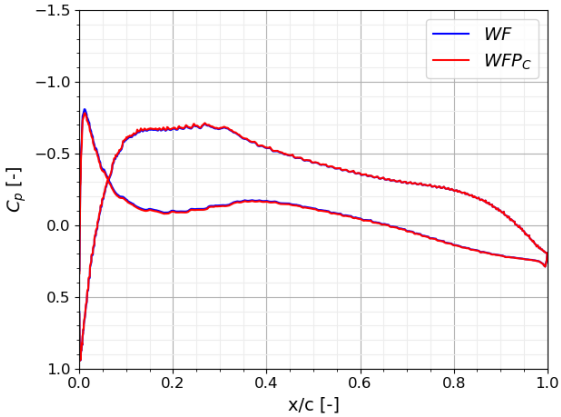

(b) y/b = 0.2

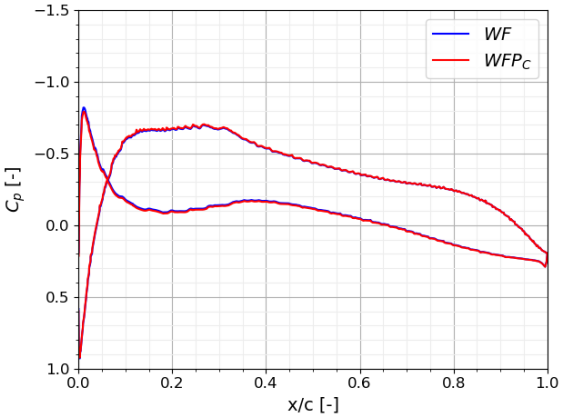

(c) y/b = 0.4

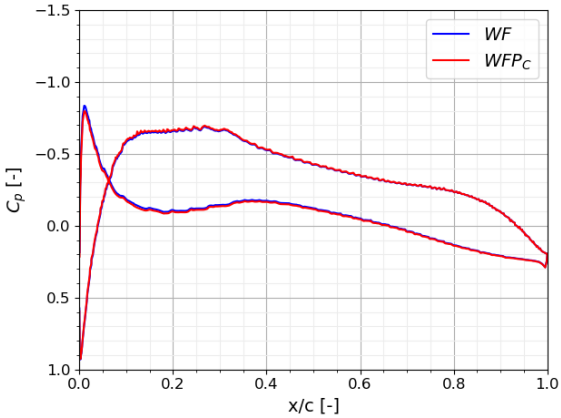

(d) y/b = 0.6

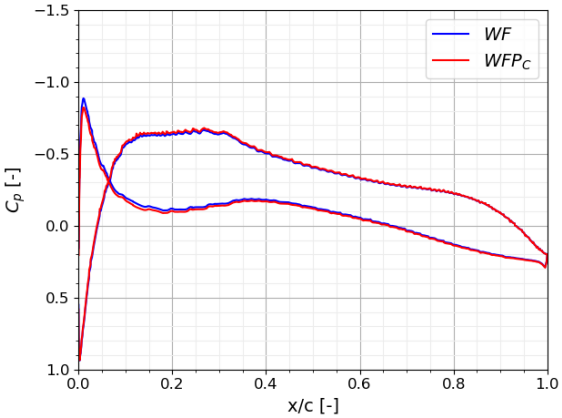

(e) y/b = 0.8

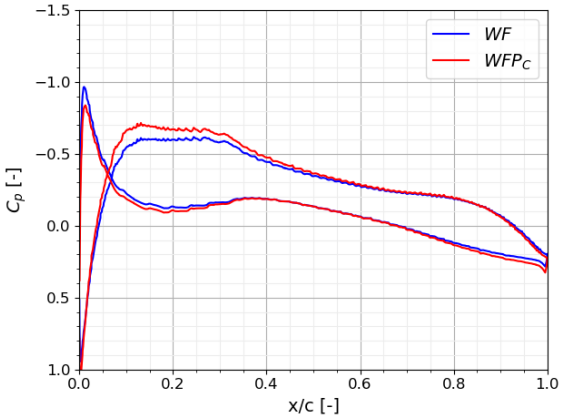

(f) y/b = 0.94

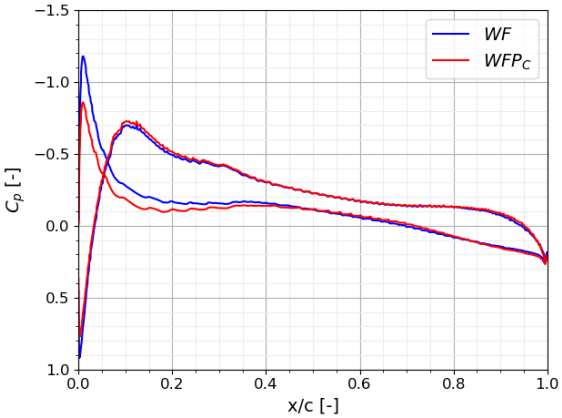

Source: Created by the author

Figure 18 – Propeller effect on the velocity contour at the wingtip for $\alpha = 0.0°$

(a) WF x/c = 0.0

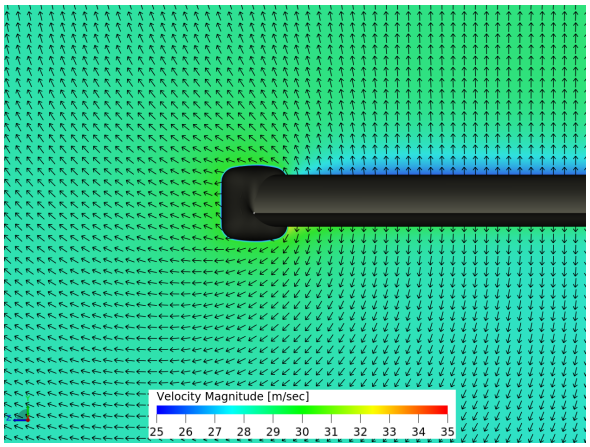

(b) WFP_C x/c = 0.0

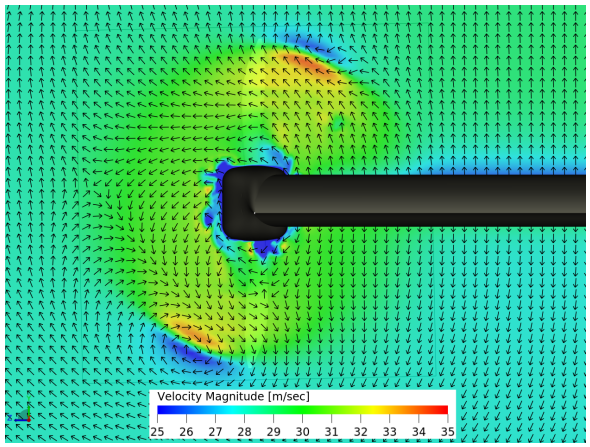

(c) WF x/c = 0.5

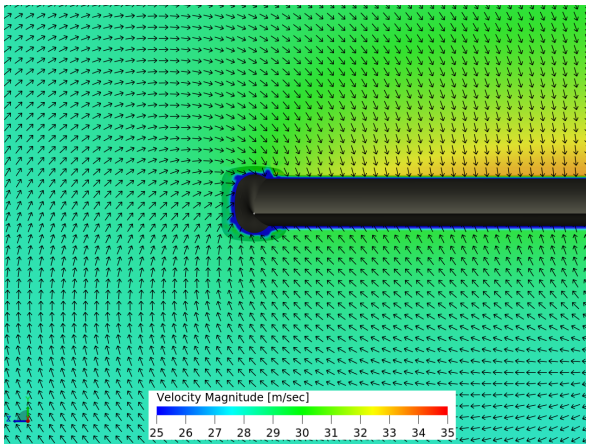

(d) WFP_C x/c = 0.5

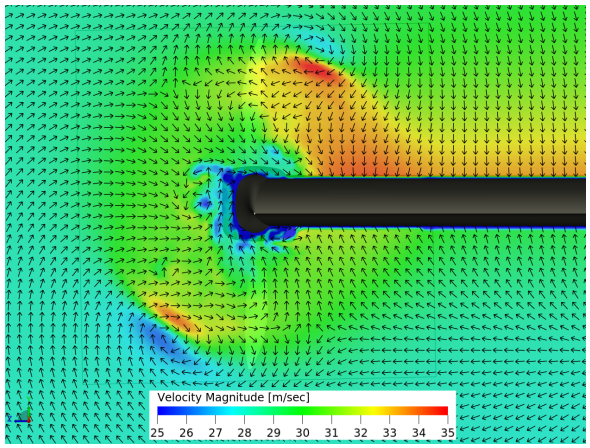

(e) WF x/c = 1.0

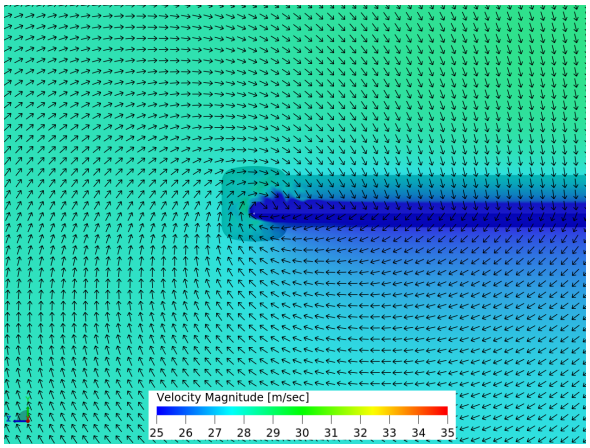

(f) WFP_C x/c = 1.0

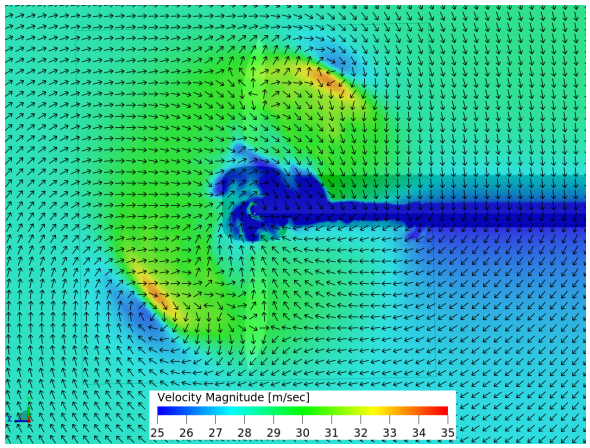

Source: Created by the author

4.3 Custom propeller

From the results up to this point, the mechanism for the reduction of induced drag through the installation of a wingtip propeller can be understood. Although gains in aerodynamic

Figure 19 – Streamlines around the wingtip for $\alpha = 0.0°$

(a) WF x/c = 0.0

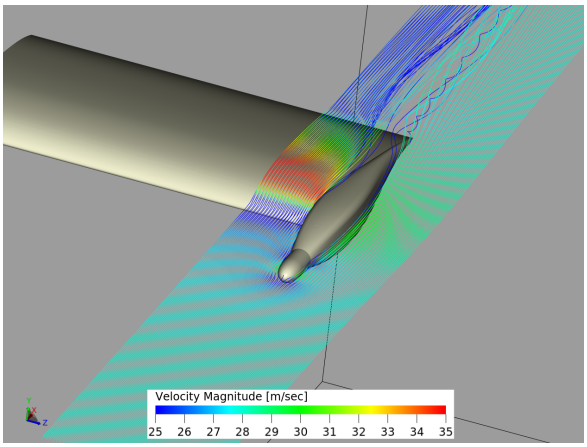

(b) WFP_C x/c = 0.0

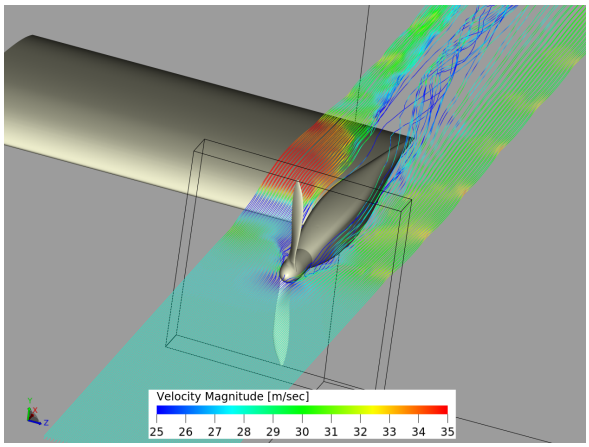

(c) WF x/c = 0.5

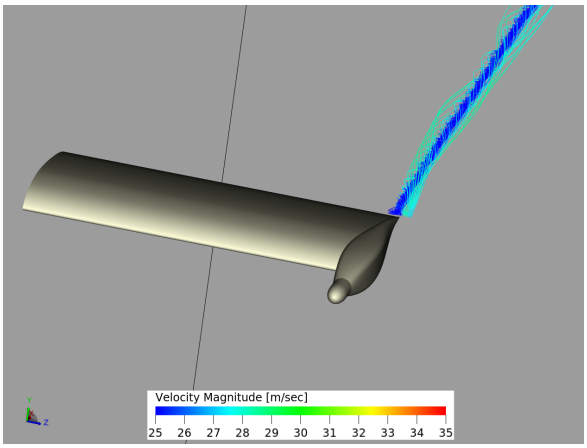

(d) WFP_C x/c = 0.5

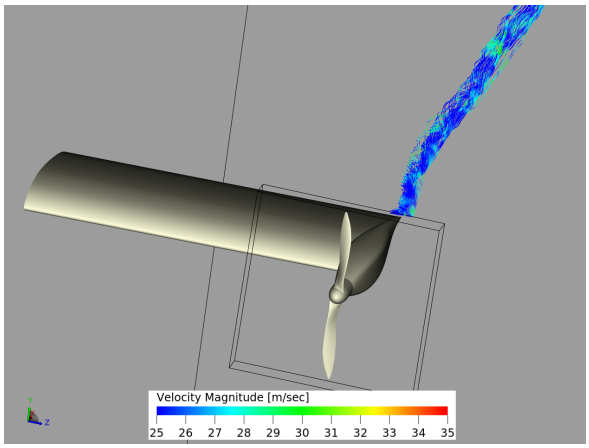

Source: Created by the author

Figure 20 – Y-Velocity at y = 0.68 m, $\alpha = 0.0°$. WF and WFP_C

(a) WF x/c = 0.0

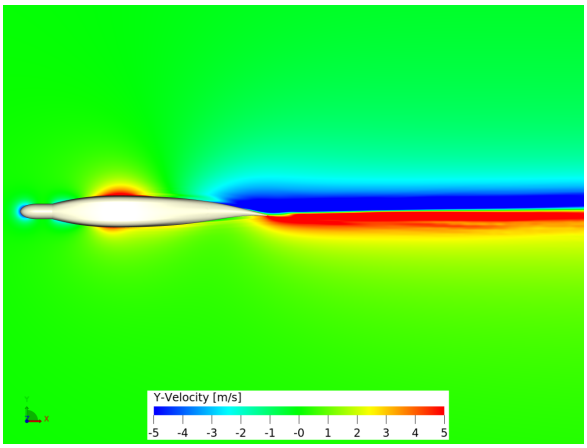

(b) WFP_C x/c = 0.0

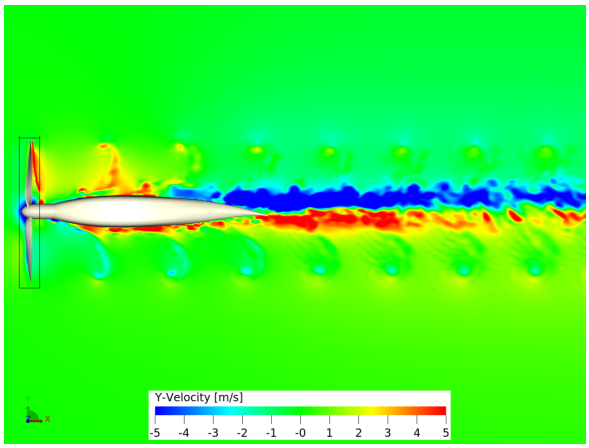

Source: Created by the author

performance have been reached, there is room for optimization when it comes to the propeller. On figure 18, it was seen that the innermost region of the propeller wake presented losses in kinematic energy, allowing for the wingtip vortex to quickly overcome the propeller swirl. Figure 21 exhibits the thrust distribution across the blades; up to 40 mm from the axis of rotation, drag is generated and, consequently, the propeller doesn't induce swirl effectively to this area.

Figure 21 – Thrust distribution across the blade

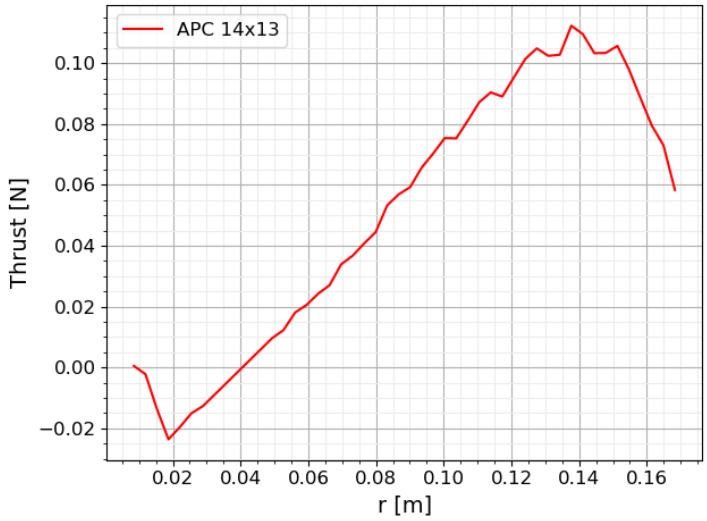

Source: Created by the author

From this observation a customized propeller was proposed. The main objective for the design was to increase the loading and the swirl closer to its axis. To achieve this, the chord and the β angle of the blade at lower radius were increased. The propeller diameter was reduced from 14 inches to 11 inches. To maintain the advance ratio equal to 1, a higher rpm must be applied, which in turn contributes to the generation of swirl. For a 11 inches, 2 blades propeller, the rotational speed necessary to achieve advance ratio close to 1 at $V_\infty = 28$ m/s is 6000 rpm.

The propeller designed was named LAE 11x11. On figure 22, the chord and β ratios between the APC 14x13 and the LAE 11x11 are presented. The CAD geometry for the modified propeller is shown on figure 23.

A wing configuration with the new propeller installed was prepared and simulated. This configuration was given the name WFP_O and its results are shown on table 4. Through figure 24, it can be seen that an improvement in performed for the WFP_O configuration was achieved. In comparison with WFP_C, the new configuration presented increased C_L and decreased C_D for all angles of attack analyzed. Regarding the induced drag, there was a further decrease on the derivative of the C_D vs. C_L^2 curve, indicating that installation of the LAE 11x11 propeller led to a larger reduction on the wingtip vortex intensity.

Figure 22 – Geometry comparison between APC 14x13 and LAE 11x11

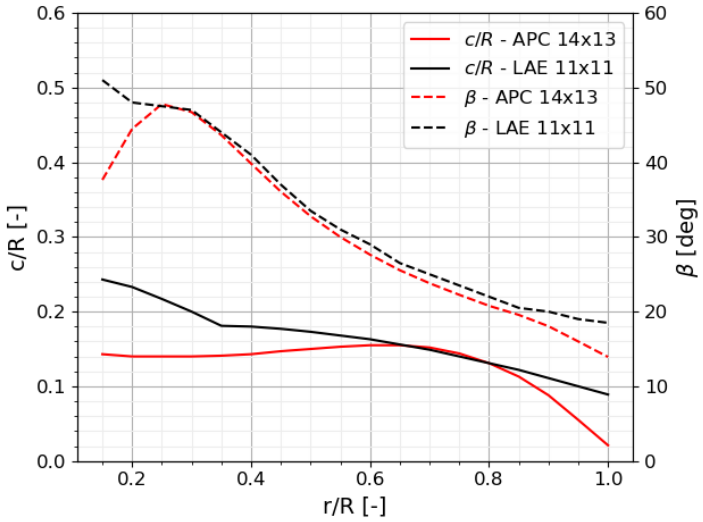

Source: Created by the author

Figure 23 – LAE 11x11 geometry

(a) Front View

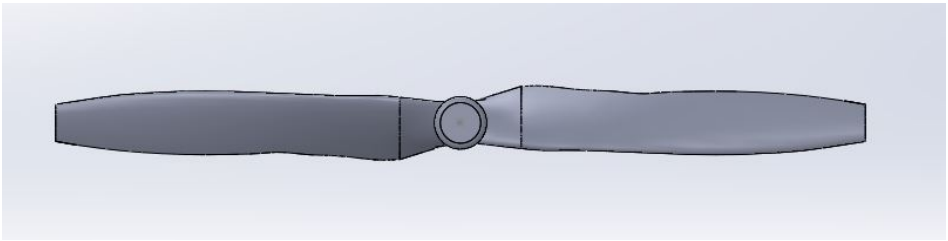

(b) Bottom View

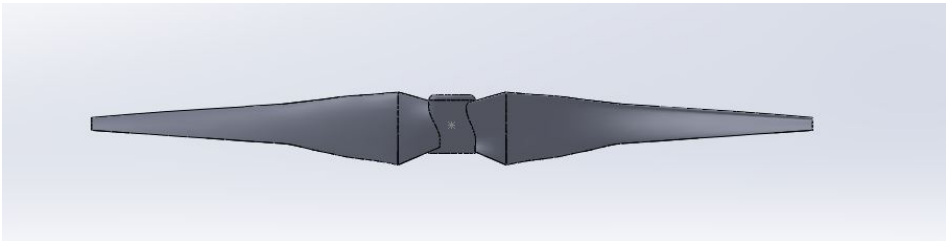

Source: Created by the author

On figure 25, the lift distribution between the three configuration are shown. For $\alpha = 0.0°$, closer to to the root, the WFP_O configuration presents slightly higher local lift in comparison with the curve for WFP_C. Directly behind the propeller wake, there is a larger offset between those curves as the LAE 11x11 propeller induced more velocity into the flow and higher α in the slipstream, as shown in figure 26.

To verify that the new propeller improved the flow field around the wingtip, the velocity

Table 4 – Results obtained from simulations, including the WFP_O configuration

Sim ID	Configuration	V_∞ [m/s]	Prop. RPM [rpm]	α [deg]	C_L [-]	C_D[-]	T [N]
01	WF	28	-	00	0.24	0.0152	-
02	WF	28	-	05	0.53	0.0378	-
03	WF	28	-	10	0.80	0.0780	-
04	WFP_C	28	4750	00	0.26	0.0159	5.27
05	WFP_C	28	4750	05	0.56	0.0380	5.28
06	WFP_C	28	4750	10	0.84	0.0790	2.00
07	WFP_O	28	6000	00	0.27	0.0154	4.48
08	WFP_O	28	6000	05	0.57	0.0375	4.68
09	WFP_O	28	6000	10	0.85	0.0779	3.84

Source – Created by the author.

contours for the WFP_C and WFP_O configurations are exhibited on figure 27. For the three plane positions, warmer colors, i.e. higher velocities, are seen close to the tip fairing, Specifically at $x/c = 0.5$, it can be seen that on the WFP_C configuration, the arrows indicates the presence of the wingtip vortex, meanwhile, on the WFP_O configuration, at this position, the wingtip vortex is not clearly formed. Therefore, the LAE 11x11 was successful in delaying the wingtip vortex formation and, consequently decreasing its intensity. Analysing the streamlines, on figure 28, the delaying of the curling motion induced by the wingtip vortex can be seen on the WFP_O configuration. It also can be seen that the flow velocities are higher around the nacelle, suggesting that less kinematic energy is lost with the LAE 11x11 propeller.

On figure 29, the velocity's y-component contours are compared. On the WFP_O configuration, the blue and red areas are slightly thinner than on the WFP_C one, indicating further weakening in the wingtip vortex. Furthermore, the blue region on the WFP_O configuration starts at a more aft position when compared to the WFP_C, what reinforces the delay of formation of the wingtip vortex.

On figure 30, the thrust distribution along the propeller radius is shown. In terms of normalized radius, the LAE 11x11 propeller presents higher loading from root to tip and the changes in chord and β decreased significantly the drag generated near the hub. Although the customized propeller has higher loading, the APC 14x13 propeller still generates more thrust due to its higher diameter.

Taking the derivative of the $CD\ vs.\ CL^2$ curves from $\alpha = 0°$ to $\alpha = 5°$ on figure 24, it is possible compare the effective aspect ratio of each configuration. On table 5, it is seen that the installation of a commercial propeller on the wingtip lead to an increase of 11% on e_0AR. The customized propeller lead to a 2% improvement over the commercial one.

Figure 24 – Aerodynamic polars for WF, WFP_C and WFP_O

(a) C_D vs. C_L

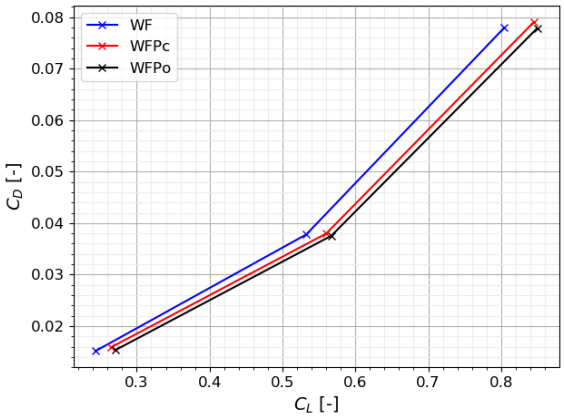

(b) C_D vs. C_L^2

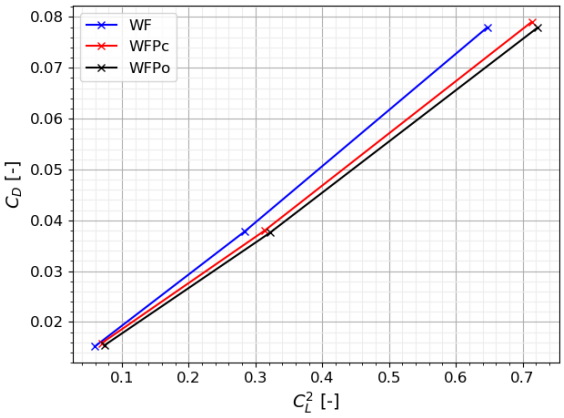

(c) C_L vs. α

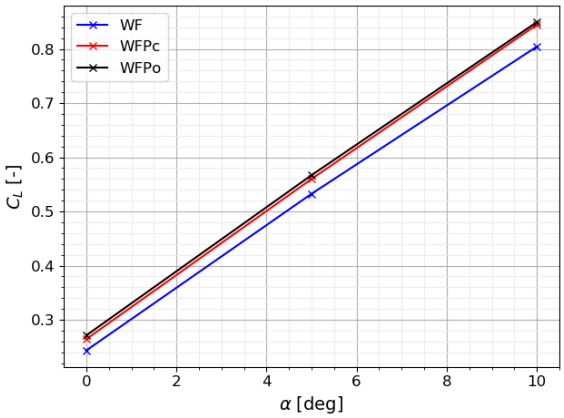

(d) L/D vs. C_L

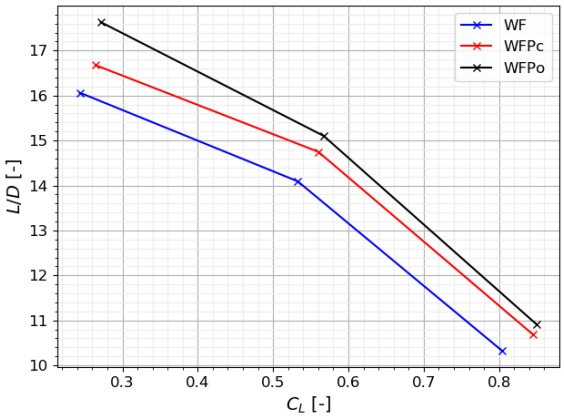

Source: Created by the author

Table 5 – Comparison of effective aspect ratio

Configuration	e_0AR [-]	Improvement %
WF	3.15	-
WFP_C	3.51	11%
WFP_O	3.56	13%

Source – Created by the author.

Figure 25 – Lift distribution for the WF, WFP_C and WFP_O configurations

(a) $\alpha = 0.0°$

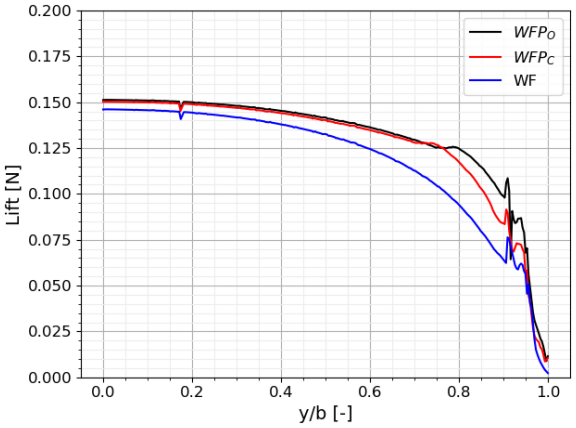

(b) $\alpha = 5.0°$

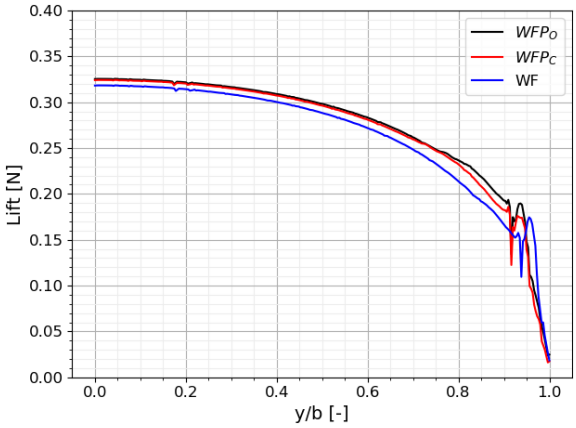

(c) $\alpha = 10.0°$

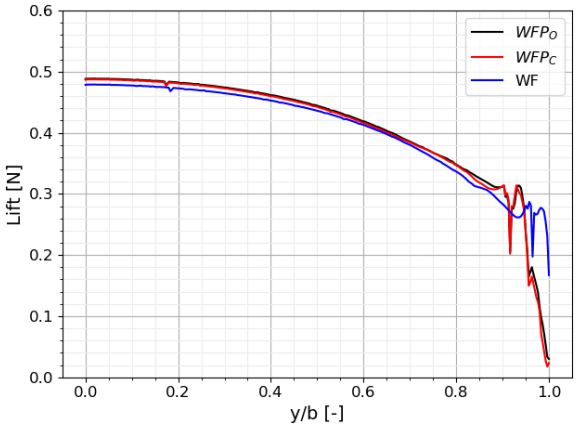

Source: Created by the author

Figure 26 – α_L 100 mm upstream of the leading edge for WF, WFP_C and WFP_O, $\alpha = 0.0°$

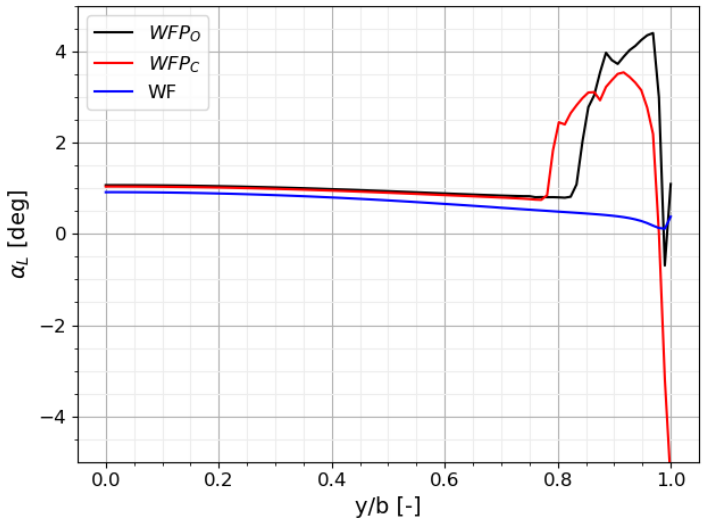

Source: Created by the author

Figure 27 – Propeller effect on the velocity contour at the wingtip for $\alpha = 0.0°$, WFP_C and WFP_O

(a) WFP_C x/c = 0.0

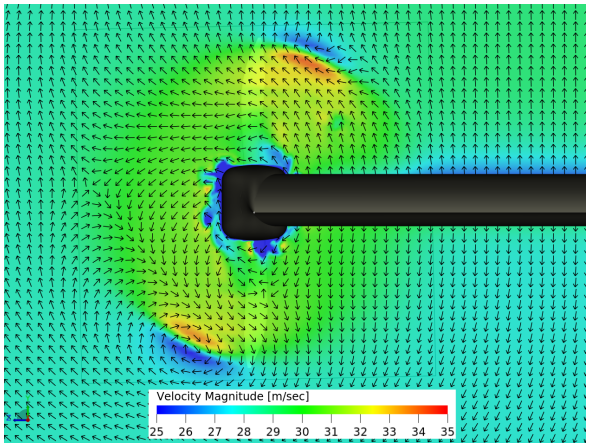

(b) WFP_O x/c = 0.0

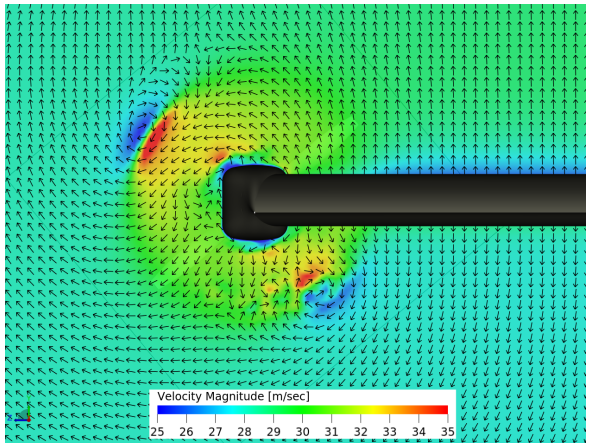

(c) WFP_C x/c = 0.5

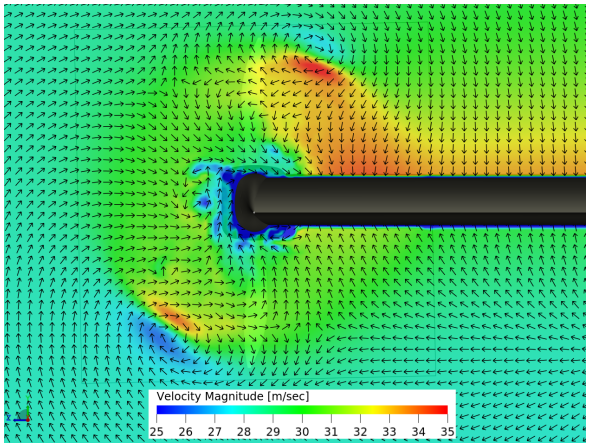

(d) WFP_O x/c = 0.5

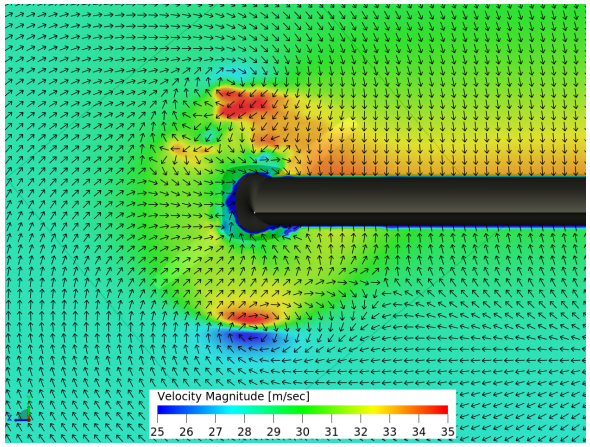

(e) WFP_C x/c = 1.0

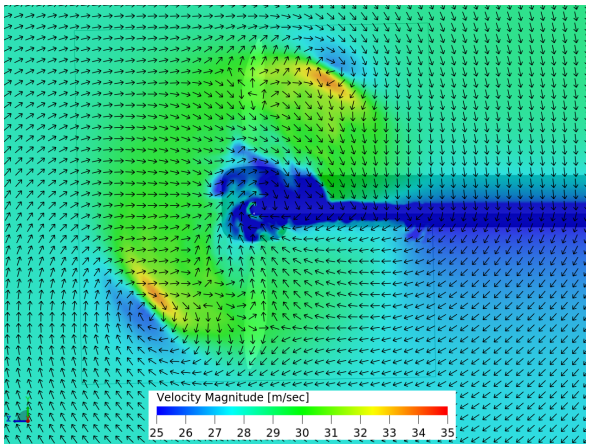

(f) WFP_O x/c = 1.0

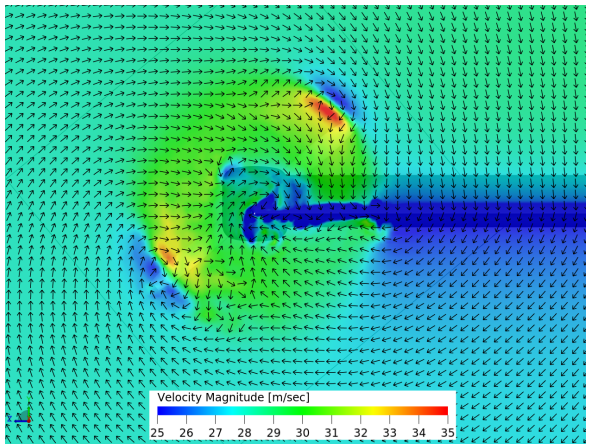

Source: Created by the author

Figure 28 – Streamlines around the wingtip for $\alpha = 0.0°$, WFP_C and WFP_O

(a) WF x/c = 0.0

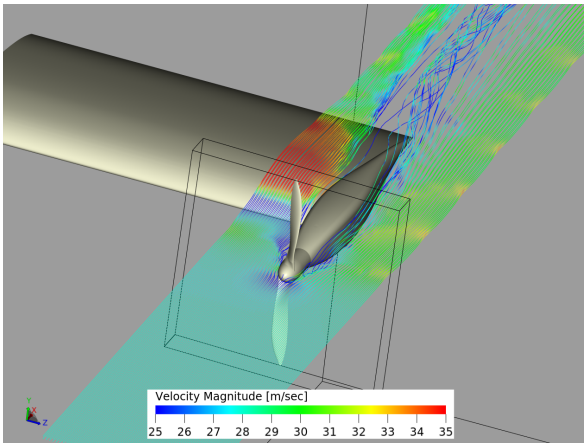

(b) WFP_C x/c = 0.0

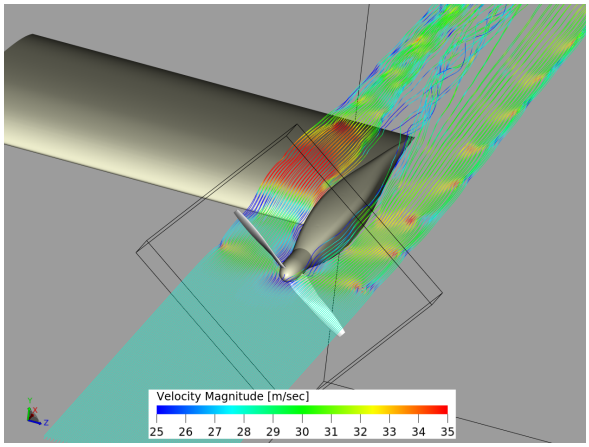

(c) WF x/c = 0.5

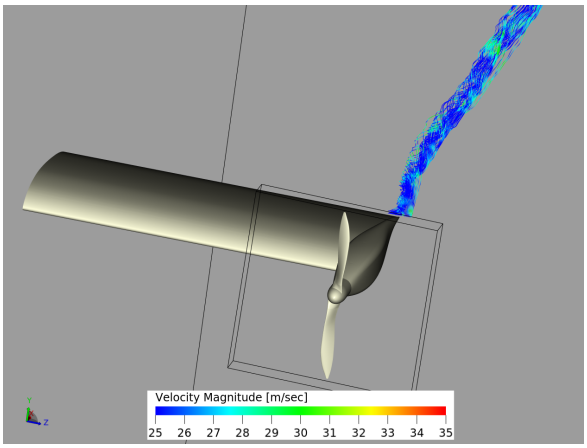

(d) WFP_C x/c = 0.5

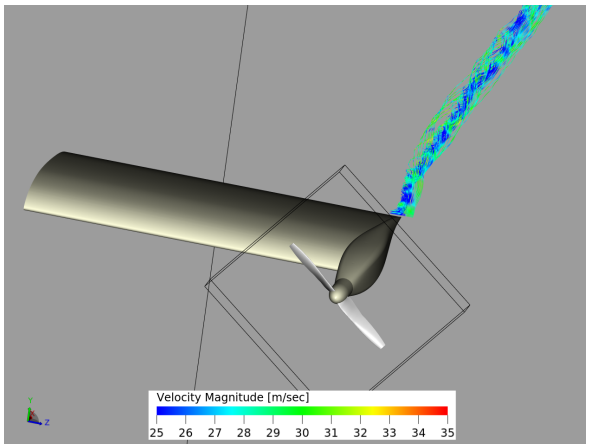

Source: Created by the author

Figure 29 – Y-Velocity at y = 0.68 m, $\alpha = 0.0°$. WFP_C and WFP_O

(a) WFP_C

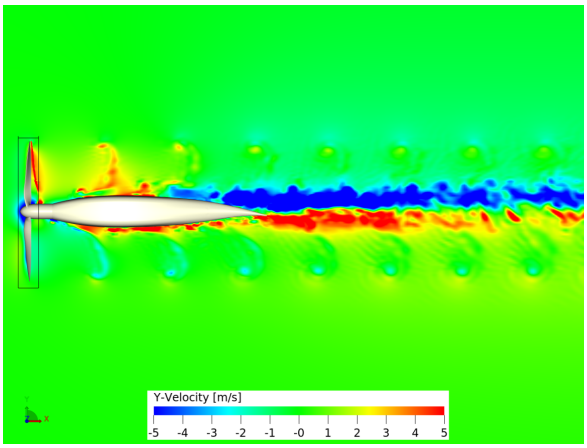

(b) WFP_O

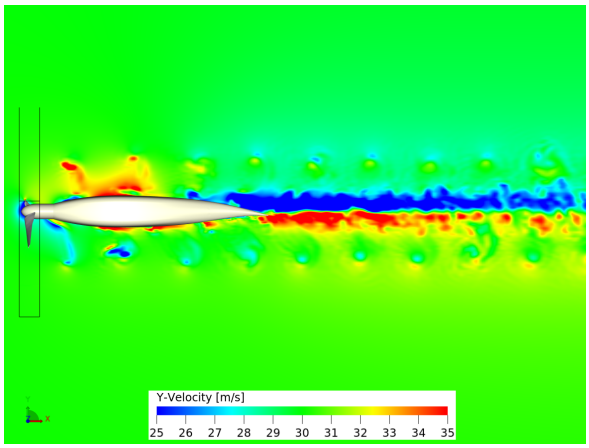

Source: Created by the author

Figure 30 – Thrust distribution comparison between APC 14x13 and LAE 11x11

(a) True Radius

(b) Normalized Radius

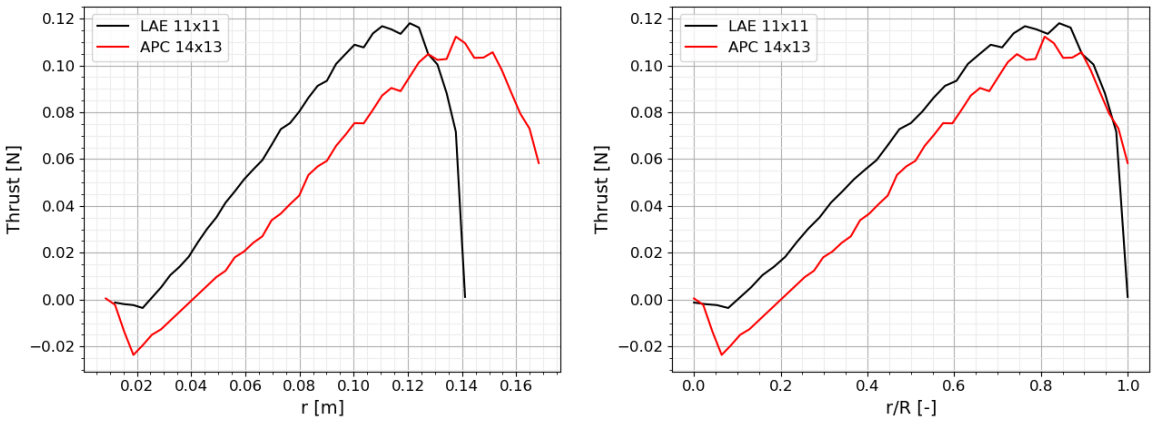

Source: Created by the author

5 CONCLUSION

The results presented on the previous section show how a counter-vortex rotating wingtip-mounted propeller affects the flow field around the wing. Its slipstream is responsible for locally increasing the angle of attack on its wake, which increases lift, and for reducing the wingtip vortex intensity simultaneously, leading to lower values of induced drag. Furthermore, it was found that adding more swirl to the slipstream near the tip improves the attenuation of the vortex.

The customized propeller proposed led to an increase in e_0AR of 2% when compared to the commercial option. Considering the modifications were made *by hand*, it can be concluded that further enhancement of the propeller can be achieved through more robust optimization methods.

One important parameter of propeller performance left out of this research is its noise generation. Regulatory agencies are becoming more strict with regards to noise due to its negative impact on human healthy and it is essential that noise constraints are met. The increase on propeller loading can lead to higher noise, as more vorticity is generated. Therefore, it's strongly recommended that a noise analysis is incorporated on the propeller optimization. Notwithstanding, the results of this work are of relevance to guide the optimization parameters from the aerodynamic perspective.

In this research, only the effects of a wingtip-mounted propeller on cruise operation have been studied. For future works, an investigation of the propeller effects on take-off and landing performance is suggested.

REFERENCES

ANDERSON, J. D. **Fundamental of Aerodynamics, 3rd Edition**. New York: McGraw-Hill, 2001. 892 p.

BORER, N. K. *et al.* Design and performance of the nasa sceptor distributed electric propulsion flight demonstrator. **16th AIAA Aviation Technology, Integration, and Operations Conference**, 2016.

DASSAULT SYSTEMES. **PowerFLOW 6-2019 user's guide**. [*S.l.: s.n.*], 2019. 104 p.

DIMCHEV, M. **Experimental and numerical study on wingtip mounted propellers for low aspect ratio UAV design**. 2012. Master Thesis — Delft University of Technology, Delft, 2012.

MIRANDA, L. R.; BRENNAN, J. E. Aerodynamic effects of wingtip-mounted propellers and turbines. **4th Applied Aerodynamics Conference - AIAA**, 1986.

MOORE, M. D.; FREDERICKS, B. Misconceptions of electric propulsion aircraft and their emergent aviation markets. **52nd Aerospace Sciences Meeting**, 2014.

NATIONAL AERONAUTICS AND SPACE ADMINISTRATION - NASA. **Systems Analysis and Concepts Directorate**. 2021. Available at: <https://sacd.larc.nasa.gov/x57maxwell/>. Access at: 27 jun. 2021.

SINNIGE, T. *et al.* Wingtip-mounted propellers: Aerodynamic analysis of interaction effects and comparison with conventional layout. **Journal of Aircraft**, v. 56, n. 1, 2018.

SMITHSONIAN. **National Air and Space Museum Collection**. 2021. Available at: <https://airandspace.si.edu/collection-objects/vought-v-173-flying-pancake/nasm_A19610120000>. Access at: 27 jun. 2021.

SNYDER, M. H.; ZUMWALT, G. W. Effects of wingtip-mounted propellers on wing lift and induced drag. **Journal of Aircraft**, v. 6, n. 5, p. 392–397, 1969.